

# Thesis not too long title

Your name goes here



Argelander-  
Institut  
für  
Astronomie

Masterarbeit in Astrophysik  
angefertigt im Argelander Institut für Astronomie

vorgelegt der  
Mathematisch-Naturwissenschaftlichen Fakultät  
der  
Rheinische Friedrich-Wilhelms-Universität Bonn  
Deutschland

May 2, 2018



*To my parents*



I hereby declare that this thesis was formulated by myself and that no sources or tools than those cited were used.

---

Date

---

Signature

1. Gutachter: Prof. Dr. (Professor Name 1)
2. Gutachter: Prof. Dr. (Professor Name 2)



# Abstract

Lorem ipsum dolor sit amet, consectetuer adipiscing elit. Etiam lobortis facilisis sem. Nullam nec mi et neque pharetra sollicitudin. Praesent imperdiet mi nec ante. Donec ullamcorper, felis non sodales commodo, lectus velit ultrices augue, a dignissim nibh lectus placerat pede. Vivamus nunc nunc, molestie ut, ultricies vel, semper in, velit. Ut porttitor. Praesent in sapien. Lorem ipsum dolor sit amet, consectetuer adipiscing elit. Duis fringilla tristique neque. Sed interdum libero ut metus. Pellentesque placerat. Nam rutrum augue a leo. Morbi sed elit sit amet ante lobortis sollicitudin. Praesent blandit blandit mauris. Praesent lectus tellus, aliquet aliquam, luctus a, egestas a, turpis. Mauris lacinia lorem sit amet ipsum. Nunc quis urna dictum turpis accumsan semper.

Lorem ipsum dolor sit amet, consectetuer adipiscing elit. Etiam lobortis facilisis sem. Nullam nec mi et neque pharetra sollicitudin. Praesent imperdiet mi nec ante. Donec ullamcorper, felis non sodales commodo, lectus velit ultrices augue, a dignissim nibh lectus placerat pede. Vivamus nunc nunc, molestie ut, ultricies vel, semper in, velit. Ut porttitor. Praesent in sapien. Lorem ipsum dolor sit amet, consectetuer adipiscing elit. Duis fringilla tristique neque. Sed interdum libero ut metus. Pellentesque placerat. Nam rutrum augue a leo. Morbi sed elit sit amet ante lobortis sollicitudin. Praesent blandit blandit mauris. Praesent lectus tellus, aliquet aliquam, luctus a, egestas a, turpis. Mauris lacinia lorem sit amet ipsum. Nunc quis urna dictum turpis accumsan semper.

Lorem ipsum dolor sit amet, consectetuer adipiscing elit. Etiam lobortis facilisis sem. Nullam nec mi et neque pharetra sollicitudin. Praesent imperdiet mi nec ante. Donec ullamcorper, felis non sodales commodo, lectus velit ultrices augue, a dignissim nibh lectus placerat pede. Vivamus nunc nunc, molestie ut, ultricies vel, semper in, velit. Ut porttitor. Praesent in sapien. Lorem ipsum dolor sit amet, consectetuer adipiscing elit. Duis fringilla tristique neque. Sed interdum libero ut metus. Pellentesque placerat. Nam rutrum augue a leo. Morbi sed elit sit amet ante lobortis sollicitudin. Praesent blandit blandit mauris. Praesent lectus tellus, aliquet aliquam, luctus a, egestas a, turpis. Mauris lacinia lorem sit amet ipsum. Nunc quis urna dictum turpis accumsan semper.

Lorem ipsum dolor sit amet, consectetuer adipiscing elit. Etiam lobortis facilisis sem. Nullam nec mi et neque pharetra sollicitudin. Praesent imperdiet mi nec ante. Donec ullamcorper, felis non sodales commodo, lectus velit ultrices augue, a dignissim nibh lectus placerat pede. Vivamus nunc nunc, molestie ut, ultricies vel, semper in, velit. Ut porttitor. Praesent in sapien. Lorem ipsum dolor sit amet, consectetuer adipiscing elit. Duis fringilla tristique neque. Sed interdum libero ut metus. Pellentesque placerat. Nam rutrum augue a leo. Morbi sed elit sit amet ante lobortis sollicitudin. Praesent blandit blandit mauris. Praesent lectus tellus, aliquet aliquam, luctus a, egestas a, turpis. Mauris lacinia lorem sit amet ipsum. Nunc quis urna dictum turpis accumsan semper.

Lorem ipsum dolor sit amet, consectetuer adipiscing elit. Etiam lobortis facilisis sem. Nullam nec mi et neque pharetra sollicitudin. Praesent imperdiet mi nec ante. Donec ullamcorper, felis non sodales commodo, lectus velit ultrices augue, a dignissim nibh lectus placerat pede. Vivamus nunc nunc, molestie ut, ultricies vel, semper in, velit. Ut porttitor. Praesent in sapien. Lorem ipsum dolor sit amet, consectetuer adipiscing elit. Duis fringilla tristique neque. Sed interdum libero ut metus. Pellentesque placerat. Nam rutrum augue a leo. Morbi sed elit sit amet ante lobortis sollicitudin. Praesent blandit blandit mauris. Praesent lectus tellus, aliquet aliquam, luctus a, egestas a, turpis. Mauris lacinia lorem sit amet ipsum. Nunc quis urna dictum turpis accumsan semper.



# Acknowledgments

Lorem ipsum dolor sit amet, consectetuer adipiscing elit. Etiam lobortis facilisis sem. Nullam nec mi et neque pharetra sollicitudin. Praesent imperdiet mi nec ante. Donec ullamcorper, felis non sodales commodo, lectus velit ultrices augue, a dignissim nibh lectus placerat pede. Vivamus nunc nunc, molestie ut, ultricies vel, semper in, velit. Ut porttitor. Praesent in sapien. Lorem ipsum dolor sit amet, consectetuer adipiscing elit. Duis fringilla tristique neque. Sed interdum libero ut metus. Pellentesque placerat. Nam rutrum augue a leo. Morbi sed elit sit amet ante lobortis sollicitudin. Praesent blandit blandit mauris. Praesent lectus tellus, aliquet aliquam, luctus a, egestas a, turpis. Mauris lacinia lorem sit amet ipsum. Nunc quis urna dictum turpis accumsan semper.

Lorem ipsum dolor sit amet, consectetuer adipiscing elit. Etiam lobortis facilisis sem. Nullam nec mi et neque pharetra sollicitudin. Praesent imperdiet mi nec ante. Donec ullamcorper, felis non sodales commodo, lectus velit ultrices augue, a dignissim nibh lectus placerat pede. Vivamus nunc nunc, molestie ut, ultricies vel, semper in, velit. Ut porttitor. Praesent in sapien. Lorem ipsum dolor sit amet, consectetuer adipiscing elit. Duis fringilla tristique neque. Sed interdum libero ut metus. Pellentesque placerat. Nam rutrum augue a leo. Morbi sed elit sit amet ante lobortis sollicitudin. Praesent blandit blandit mauris. Praesent lectus tellus, aliquet aliquam, luctus a, egestas a, turpis. Mauris lacinia lorem sit amet ipsum. Nunc quis urna dictum turpis accumsan semper.

Lorem ipsum dolor sit amet, consectetuer adipiscing elit. Etiam lobortis facilisis sem. Nullam nec mi et neque pharetra sollicitudin. Praesent imperdiet mi nec ante. Donec ullamcorper, felis non sodales commodo, lectus velit ultrices augue, a dignissim nibh lectus placerat pede. Vivamus nunc nunc, molestie ut, ultricies vel, semper in, velit. Ut porttitor. Praesent in sapien. Lorem ipsum dolor sit amet, consectetuer adipiscing elit. Duis fringilla tristique neque. Sed interdum libero ut metus. Pellentesque placerat. Nam rutrum augue a leo. Morbi sed elit sit amet ante lobortis sollicitudin. Praesent blandit blandit mauris. Praesent lectus tellus, aliquet aliquam, luctus a, egestas a, turpis. Mauris lacinia lorem sit amet ipsum. Nunc quis urna dictum turpis accumsan semper.

Lorem ipsum dolor sit amet, consectetuer adipiscing elit. Etiam lobortis facilisis sem. Nullam nec mi et neque pharetra sollicitudin. Praesent imperdiet mi nec ante. Donec ullamcorper, felis non sodales commodo, lectus velit ultrices augue, a dignissim nibh lectus placerat pede. Vivamus nunc nunc, molestie ut, ultricies vel, semper in, velit. Ut porttitor. Praesent in sapien. Lorem ipsum dolor sit amet, consectetuer adipiscing elit. Duis fringilla tristique neque. Sed interdum libero ut metus. Pellentesque placerat. Nam rutrum augue a leo. Morbi sed elit sit amet ante lobortis sollicitudin. Praesent blandit blandit mauris. Praesent lectus tellus, aliquet aliquam, luctus a, egestas a, turpis. Mauris lacinia lorem sit amet ipsum. Nunc quis urna dictum turpis accumsan semper.

Lorem ipsum dolor sit amet, consectetuer adipiscing elit. Etiam lobortis facilisis sem. Nullam nec mi et neque pharetra sollicitudin. Praesent imperdiet mi nec ante. Donec ullamcorper, felis non sodales commodo, lectus velit ultrices augue, a dignissim nibh lectus placerat pede. Vivamus nunc nunc, molestie ut, ultricies vel, semper in, velit. Ut porttitor. Praesent in sapien. Lorem ipsum dolor sit amet, consectetuer adipiscing elit. Duis fringilla tristique neque. Sed interdum libero ut metus. Pellentesque placerat. Nam rutrum augue a leo. Morbi sed elit sit amet ante lobortis sollicitudin. Praesent blandit blandit mauris. Praesent lectus tellus, aliquet aliquam, luctus a, egestas a, turpis. Mauris lacinia lorem sit amet ipsum. Nunc quis urna dictum turpis accumsan semper.



# Contents

<b>Abstract</b>	vii
<b>Acknowledgments</b>	ix
<b>Contents</b>	xi
<b>List of Figures</b>	xiii
<b>List of Tables</b>	xv
<b>1 Introduction</b>	1
1.1 Low frequency astronomy . . . . .	1
1.1.1 LOw Frequency array- LOFAR . . . . .	2
1.1.2 Radio Interferometry Measurement Equation- RIME formalism . . . . .	4
1.1.3 Overview of imaging procedure for LOFAR . . . . .	6
1.1.4 Importance of low frequency astronomy (LOFAR Key Science Projects) . . . . .	7
1.2 Mechanisms important at Low Frequencies . . . . .	8
1.2.1 Synchrotron emission: . . . . .	8
<b>2 Imaging</b>	11
2.1 NGC628 . . . . .	11
2.2 IC342 . . . . .	11
2.3 Observational setup . . . . .	13
2.4 Calibration of LOFAR data . . . . .	14
2.4.1 Direction independant part . . . . .	14
2.4.2 Direction dependant part . . . . .	14
2.4.3 Overview of Factor . . . . .	16
2.5 Imaging . . . . .	18
<b>A Appendix not too long title</b>	23
<b>Bibliography</b>	23



# List of Figures

1.1	The different Antenna types in LOFAR. <i>Left:</i> Low Band Antenna is held upright by the two copper wires connected to its top that help in detection of the two polarisations, and the ground mesh (?). <i>Right:</i> Each High Band Antenna tile has 16 aluminium elements held together by an expanded polystyrene structure (?) . . . . .	2
1.2	Arrangement of the LOFAR stations in Europe. <i>Left:</i> The blue regions represent the international stations. The orange regions in the represent the remote stations. <i>Right:</i> On a closer look, the red regions represent the core stations. These images were obtained from <a href="http://astron.nl/lofar/tools/lofarmap.html">http://astron.nl/lofar/tools/lofarmap.html</a> . . . . .	3
1.3	The uv coverage of LOFAR including all core, remote and international stations (?). The simulation of this uvcoverage is based on a hypothetical 6 hour observation of a source at a declination of 48 deg between 30-78 MHz using single beam with bandwidth of 48 MHZ . . . . .	4
1.4	This is the Spectral Energy Distribution of M82, a starburst galaxy. The region below the frequency of 30 GHz is from non-thermal, synchrotron emission from cosmic ray electrons. Below that frequency, free-free emission from HII regions dominates, until $\sim$ 200 GHz (?) . . . . .	7
1.5	This is a schematic diagram depicting the lifetime of our universe. At redshift $z \approx 1100$ , the dark ages begin, and EoR begin at $z \approx 6-12$ . Courtesy of National Astronomical Observatory of Japan (NAOJ) . . . . .	8
1.6	When an electron moves at relativistic speeds, the $\sin^2$ radiation pattern is Lorentz transformed. <i>Left:</i> The radiation pattern of a non-relativistic electron. <i>Right:</i> The relativistic radiation pattern. This image has been taken from <a href="http://www.astro.utu.fi/\protect\unhbox\voidb@x\penalty\OM\{cflynn/astroII/14.html">http://www.astro.utu.fi/\protect\unhbox\voidb@x\penalty\OM\{cflynn/astroII/14.html</a> . . . . .	9
2.1	Schematic of the chemical and physical structure of the nucleus of IC 342(?) . . . . .	12
2.2	This was the arrangement of baselines used for the observation. This is a plot generated by task in CASA called 'plotms' for the first measurement set for the frequency 111 MHz in the first time step. From the plot, one can see the baselines used in terms of meters. As can be seen, the observation uses a dense core to image diffuse flux in the galaxy- the disk and the halo parts. <i>Right:</i> This image shows the shorter baselines used. The shortest projected baseline used was around 23 m. . . . .	13
2.3	<i>Left:</i> Initial subtract image of NGC628, using frequencies between 135 to 167 MHz. It has a restoring beam of 43.99 arcsec by 31.64srcsec and position angle of -17.27deg. As can be seen, artifacts from individual sources, such as 3C 049 (at RA: 01h41m09.160s and DEC: +13d53m28.05s in J2000 coordinate system), can severely affect the galaxy image quality. Hence, the field of view is divided into "isoplantic" patches called "facets". <i>Right:</i> The facet patches can be seen in the image, and are made around the radio sources present in each facet. They are represented by the white dots in the image on the right. The facet patches are based on the Veroni tessellation scheme. . . . .	15
2.4	This image depicts the faceting scheme used for NGC628. The middle facet marked "target" is NGC628. The sources marked 1, 4 and 5 were included by hand due to their high fluxes. The image is the one obtained from the initial calibration (same as the one in the previous figure). The beam is elongated to account for the low elevation elongation of the LOFAR primary beam. . . . .	16
2.5	Self calibration images of the facet with source 194- otherwise known as 3C49. The image marked "Dir. Independ." is the direction independant image of the facet. In the second row, the phase term is being solved, which took three iterations. Then, the phase + amplitude calibration was done, which took 7 iterations. . . . .	17

2.6	<i>Left:</i> The initial subtract image of facet containing the source 3C49. <i>Right:</i> Final self-cal image of 3C49. The image is considerably better than the one on the left,however some of the artifacts still remain. The source is the source is farther away from the target source, hence, the artifacts that remain do not affect the image too much. . . . .	18
2.7	Faceting in IC342 for Direction Dependant calibration in Factor. The facets have been overlaid on the image made using averaged Prefactor data. The resolution of the image is 17.35 by 12.72 arcsec. It was cleaned to a threshold of 0.3 mJy with Briggs weighting of -0.5. . . . .	19
2.8	This is the LOFAR image of IC342 at the central frequency of 146.2 MHz. Bandwidth of the observation was 62.5 MHz. This image has the resolution of 12.48" by 10.26"; PA: -8.10 deg. The contours are at 3, 8, 12, 18, 18, 32 and 44 of 0.3 mJy/beam, which is the noise of the image in a quiet region. . . . .	19
2.9	This image has the resolution of 25.93" by 23.26"; PA: 62.7 deg. The contours are at 3, 8, 12, 18, 18, 32 and 44 of 0.43 mJy/beam. . . . .	21
2.10	This image has the resolution of 38.15" by 34.39"; PA: 23.99 deg. The contours are at 3, 8, 12, 18, 18, 32 and 44 of 0.6 mJy/beam. . . . .	21

# List of Tables

1.1	LOFAR specifications, all obtained from (?) . . . . .	3
1.2	The LOFAR imaging modes . . . . .	4
2.1	Parameters of NGC628 . . . . .	11
2.2	Parameters of IC342 . . . . .	12
2.3	Parameters of NGC628 . . . . .	13
2.4	This table shows the diagnostic plots that are obtained as an output from the Prefactor pipeline. They give an overview of the condition of the data and help us select and flag any data sets that seem bad, and were not previously flagged by the pipeline. . . . .	20



# Chapter 1

## Introduction

### 1.1 Low frequency astronomy

#### History of radio astronomy

- |       |   |
|-------|---|
| 1933  | At the Bell Labs, Karl Jansky was trying to figure out the source of interference at short wavelength in the transatlantic wireless communication, and discovered radiation at 20.5 MHz frequency that moved across our sky and figured out that it was not from earth.   |
| 1937  | Grote Weber speculated that these signals were thermal in nature and built a parabolic reflector radio telescope with a diameter of 9.5 m and made the first radio map depicting the galactic plane and parts of the sky at 160 MHz, and published the paper (?) in 1944.   |
| 1940s | Innovations during the Second World War in the RADAR technology further helped the research J.S. Hey, England and G. C. Southworth discovered that sun was radiating radio emission. This was followed by discovery of fluctuation in cosmic radiation at radio frequency by J.S. Hey, S.J. Parsons, and J.W. Phillips (?). Several discrete radio sources were also identified. Radio emission from meteors was also studied.      |
| 1950s | In the paper (?), H. I. Ewen and E. M. Purcell observed the H1 21 cm line from galaxy, as predicted by van de Hulst in 1945. Several radio observatories came to life in this such as Cambridge observatory that helped in producing the 2C and 3C catalogues, and was the decade first to make use of aperture synthesis technique. Radio emission from Jupiter was also studied at 22 MHz and 3 GHz (?).                          |
| 1960s | A. Penzias and R. Wilson using the Holmdel Horn Antenna at the Bell Labs made one of the most important astrophysical discoveries: the Cosmic Microwave Background, for which they were awarded the Nobel prize in 1978. This decade also marked the discovery of pulsars by J. Bell in her article "Little Green Men, White Dwarfs or Pulsars?" (?) Sir M. Ryle and A. Hewish received the Nobel prize in 1974 for this discovery. |
| 1970s | Hulse and Taylor discovered the first binary pulsar system at Arecibo, and thus proved the presence of Gravitational wave radiation, after conducting pulsar timing for nearly 20 years (?). They were awarded the Nobel prize for this discovery in 1993.<br>The first global radio telescope was formed, in 1976 to observe water maser sources.  |
| 1980s | The need to better resolution gave rise to construction of interferometers such as TPT in Clark Lake observing at the frequency of 57.5 MHz. The first self calibration for VLA images was done. Astronomical Image Processing Software (AIPS) was released.  |
| 1990s | VLA system observing at 74 MHz frequency was used. Planck black-body spectrum for the CMB was measured, and the anisotropy was discovered for the first time using COBE satellite. (?) Mather and G. Smoot were awarded Nobel prize for this discovery in 2006.   |

Due to the need for higher resolutions, studies were mostly focussed on higher frequencies<sup>1</sup> during 1970 to

<sup>1</sup>Angular resolution of a single dish telescope can be written as  $\theta = \alpha \frac{\lambda}{d}$  rad, where ‘ $\lambda$ ’ is the wavelength of observation and ‘ $d$ ’ is the diameter of the telescope (both in terms of meters). In case of an interferometer, the resolution is written as  $\theta = \alpha \times \frac{\lambda}{D}$  rad, where  $D$  is the distance between the telescopes (in meters). Here  $\alpha$  depends on the array configuration and the weighing scheme used during

2000. Several higher frequency telescopes were made- VLA, ATCA, GMRT, MERLIN and single dish telescopes such as Effelsberg, Arecibo and Lovell. Interest in low frequency radio astronomy begin when many sources were seen to have inverted spectra due to synchrotron self-absorption or free-free absorption<sup>2</sup>. NRAO and the Naval Research Laboratory completed the implementation of a VLA at 73.8 MHz in 1998 and found that ionospheric phase shifts posed the biggest difficulty in calibrating data. It was found that self-calibration could help with this (?). In the paper (?), 70,000 sources were catalogues including several extra-galactic and galactic sources such as high redshift galaxies, galaxy clusters, pulsars and Supernovae Remenants (SNRs) at 77 MHz. It covers almost 95% of the  $3\pi$  sr of sky above -30 deg declination. This survey is very useful for calibration in LOFAR. This survey has been revised to give 95,000 sources in (?). In the paper (?), a  $1 \text{ km}^2$  array was proposed so as to study the neutral hydrogen at cosmological distances, called the Square Kilometer Array (SKA). Due to cost constraints, the concept of Phased Arrays (?) using dipole antennae was proposed, which then gave rise to LOFAR.

### 1.1.1 LOW Frequency array- LOFAR

LOFAR or LOw Frequency Array is a radio interferometer mainly located in the Netherlands. It consists of two types of receiving elements: the Low Band Antennae (LBA) that covers the frequency range of 10-90 MHz, and the High Band Antennae (HBA) that covers the frequency range from 110-250 MHz. It is interesting to note that the pointing in LOFAR is done by applying digital delays to elements of individual stations. The LBA (shown in Fig. 1.1a) in reality can only operate between the frequency range of 30-80 MHz due to the presence of Radio Frequency Interference(RFI) at the lower frequency regime and the commercial FM band at the higer regime. An LBA dipole can detect two orthogonal linear polarisations, with an all-sky sensitivity. The dipoles themselves do the make up the elements to do beamforming. The HBA (shown in Fig. 1.1b) can reach frequency only upto 240 MHz due to RFI. 16 antennae are grouped under one “tile”, and each of these tiles can form a “tile beam”. Each tile does the beamforming with the help of an analogue beamformer that adds a delay to each dipole.



Figure 1.1: The different Antenna types in LOFAR. *Left:* Low Band Antenna is held upright by the two copper wires connected to its top that help in detection of the two polarisations, and the ground mesh (?). *Right:* Each High Band Antenna tile has 16 aluminium elements held together by an expanded polystyrene structure (?)

It has a dense core i.e., it has numerous short baselines that are very helpful in the study of diffuse emission. LOFAR currently has 24 core stations (CSs) located in Exloo, Netherlands, and 14 remote stations (RSs) located all over the Netherlands. These stations have 96 LBAs and 48 HBAs with 48 digital Receiver Units (RCUs). These arragements can be seen the Fig. 1.2. The international stations (ISs) are present in Germany (5 stations), Great Britain (1 station), France (1 station) and Sweden (1 station). A summary of the arrangement and other properties of LOFAR are given in Table 1.1.

The data from both LBA and HBAs are sent to the receiver unit (RCU), where digitisation happens through coaxial cables. Then the beam-forming is done int he digital electronics section. After that, the signal is either sent to the Cobalt correlator in Groningen or recorded and delt with locally based on the observing mode. LOFAR has three main observing modes that are explained in the Table 1.2.

The data streams from the individual dipole antennae are sent to the Central Processing (CEP) facility located in Groningen through a dedicated network high speed fibres. The data is then processed in the Blue Gene/P supercomputer. During this processing, the signal from the stations is correlated, and the beam-forming is done. After this, the data is given to the storage cluster. The data is processed using several reduction pipelines before

imaging ???. In reality, it also depends on the array configuration and the declination of the source. For LOFAR, the resolution varies between 0.5deg to sub-arcsecs.

<sup>2</sup>We will visit these phenomena in section ??.

Characteristic	Value	Comments
Frequency range	10-90 MHz	LBA
	110-190 MHz	HBA
Shortest baseline	68m	among CSs, RSs and ISs (unprojected values)
Maximum baseline	3.5 km	CSs
	121 km	RSs
	1158 km	ISs
Number of Polarisations	2	
Bandwidth	48 MHz	16-bit mode
	96 MHz	8-bit mode
Maximum number of simultaneous beams	244	16-bit mode
	488	8-bit mode

Table 1.1: LOFAR specifications, all obtained from (?)

Figure 1.2: Arrangement of the LOFAR stations in Europe. *Left:* The blue regions represent the international stations. The orange regions in the represent the remote stations. *Right:* On a closer look, the red regions represent the core stations. These images were obtained from <http://astron.nl/lofar/tools/lofarmap.html>

being stored in the LOFAR long term archive (LTA) for scientific purposes. The CEP4 cluster, part of the LOFAR clusters, is used to do the initial processing and calibration using pipelines on the data from the Cobalt correlator (in Groningen). Another cluster- CEP3, used by LOFAR users to decide the strategy to be used for calibration. Once the data has been processed, it is made available on Long Term Archive (LTA).

Some of the packages used for the calibration of LOFAR data are: Astronomical Image Processing Software(AIPS) (?), Common Astronomy Software Applications (CASA) (?), AOFlagger (helps in flagging RFI) (?), SAGECal (calibration package), dysco (compressing storage manager for measurement sets) and several others, which will be visited upon during the course of the thesis.

Some of the performance metrics of LOFAR are described below:

- The rate of change of the ionospheric phase above Netherlands is 1rad per 15s in the 110 to 190 MHz band (?). For LBA, water may affect the gain by the order of 10%, though HBA amplitudes remain pretty stable. These effects of ionospheric phase shift can be significantly depreciated using the method of self- calibration ??.
- The angular resolution of the observation depends on the declination of the source, and the array configuration. For LOFAR, it is from 0.5 deg to sub-arcsec levels.
- One factor that affects the image quality is the uv coverage. As can be seen from the Fig.1.3, we can easily see that LOFAR has a very dense core and there are several long baselines, for better resolution.

Modes	Description
Interferometric	Gives visibility data to be used in surveys and for single source imaging.
Beam Formed	This is used when high time resolution is needed e.g., for pulsars, cosmic rays, etc.
Direct Storage	Uncorrelated data is recorded locally for single station all sky imaging or local Trasient Buffer Board (TBB) experiments.

Table 1.2: The LOFAR imaging modes

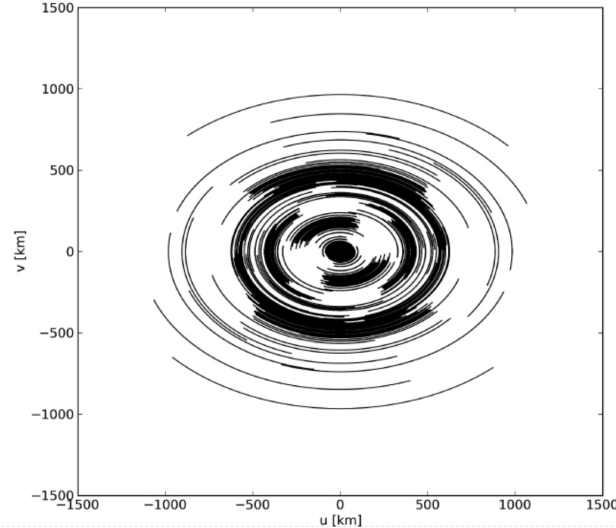


Figure 1.3: The uv coverage of LOFAR including all core, remote and international stations (?). The simulation of this uvcoverage is based on a hypothetical 6 hour observation of a source at a declination of 48 deg between 30-78 MHz using single beam with bandwidth of 48 MHZ

- The bandpass of LOFAR is affected by several factors: the station beam- which is in itself frequency dependent, the interaction between the antenna elements and the low noise amplifier (LNA). Inorder to take care of this, a digital correction is applied within each 0.2 MHz subband.
- The Field of View of LOFAR ranges from 2 to 1200 deg<sup>2</sup>, and is given by:

$$\text{FoV} = \pi \left( \frac{FWHM}{2} \right)^2 \quad (1.1)$$

### 1.1.2 Radio Interferometry Measurement Equation- RIME formalism

The calibration techniques used for LOFAR are based on RIME formalism, which is explained in the section 1.1.2. The explaination closely follows the one given in (?), since the Direction Dependant Effects (DDE) are well explained in it. This section describes the calculation of RIME from the voltages obtained at the antennae.

Consider a quasi-monochromatic source giving out a signal. This can be represented by a complex vector  $\mathbf{e}$  (the “original signal”), and be written in the form of a matrix using an orthogonal coordinate system  $xyz$ , with ‘z’ along the direction of propagation.

$$\mathbf{e} = \begin{pmatrix} e_x \\ e_y \end{pmatrix}$$

The signal encounters multiple effects on its path towards the antennae. These effects are assumed to affect the signal **linearly**. The signal changes to  $\mathbf{e}'$  due to these effects and can be written in the form given in the equation 1.2.

$$\mathbf{e}' = \underbrace{\mathbf{J}_n \mathbf{J}_{n-1} \dots \mathbf{J}_1}_{\text{Jones chains}} \mathbf{e} = \mathbf{J} \mathbf{e} \quad (1.2)$$

Here,  $\mathbf{J}$  is a  $2 \times 2$  complex matrix known as Jones matrix. Since there are multiple effects along the path of the signal, the Jones chain is written taking all these effects into account and the final cumulative Jones matrix can be written as  $\mathbf{J}$ .

If  $a$  and  $b$  are two linear dipole feeds, the signal one reaching and gets converted to complex voltages  $v_a$  and  $v_b$  representing the two polarisations.

$$\mathbf{v} = \begin{pmatrix} v_a \\ v_b \end{pmatrix} = \mathbf{J} \mathbf{e} \quad (1.3)$$

An interferometer consists of several antennae elements, so let us consider two such spatially separated elements -  $p$  and  $q$ , giving independent voltage vectors  $v_p$  and  $v_q$ . Their voltages are correlated to give the visibility matrix  $V_{pq}$ . Hence, the visibility matrix can be written as:

$$V_{pq} = 2 \begin{pmatrix} \langle v_{pa} v_{qa}^* \rangle & \langle v_{pa} v_{qb}^* \rangle \\ \langle v_{pb} v_{qa}^* \rangle & \langle v_{pb} v_{qb}^* \rangle \end{pmatrix}$$

Here,  $v^*$  represents the complex conjugate of  $v$ .  $V_{pq}$  can be written as matrix product of  $v_p$  and complex conjugate of  $v_q$ .  $H$  represents the conjugate transpose operation.

$$V_{pq} = 2 \langle v_p v_q^H \rangle \quad (1.4)$$

Combining equations 1.3 and 1.4, we get:

$$V_{pq} = 2 \langle \mathbf{J}_p (\mathbf{e} \mathbf{e}^H) \mathbf{J}_q \rangle \quad (1.5)$$

We assume that  $\mathbf{J}_p$  and  $\mathbf{J}_q$  are constant over the averaging interval.

$$V_{pq} = 2 \langle v_p v_q^H \rangle = 2 \mathbf{J}_p \begin{pmatrix} \langle e_x e_x^* \rangle & \langle x_x e_y^* \rangle \\ \langle e_y e_x^* \rangle & \langle e_y e_y^* \rangle \end{pmatrix} \mathbf{J}_q^H \quad (1.6)$$

A relation can be obtained between the source signal and Stokes parameters (I, Q, U, V) as shown in (?), and a new matrix called the brightness matrix B is defined.

$$2 \begin{pmatrix} \langle e_x e_x^* \rangle & \langle x_x e_y^* \rangle \\ \langle e_y e_x^* \rangle & \langle e_y e_y^* \rangle \end{pmatrix} = \underbrace{\begin{pmatrix} I + Q & U + iV \\ U + iV & I - Q \end{pmatrix}}_{\text{Brightness matrix B}} \quad (1.7)$$

The signal undergoes sequential layers of corruption, and the resulting Jones matrix  $\mathbf{J}_p$  can be written in the form of Jones chain:  $\mathbf{J}_p = (\mathbf{J}_{pn} \cdot \mathbf{J}_{p(n-1)} \dots \mathbf{J}_{p1})$ .

The final Jones matrix can be thus written as a cumulative of the following terms:

- The **phase** term: Phase difference exists between the two antennae due to the pathlength difference between the paths from source to  $p$  and  $q$ . This in turn corrupts the signal. Phase centre is the direction in which the antennae are steered towards to minimise the phase difference<sup>3</sup>.

Considering the conventional coordinate system, with  $z$  axis pointed towards the phase center, antenna  $p$ 's location can be defined as  $\mathbf{u}_p = (u_p, v_p, w_p)$ . Thus, the phase term in Jones matrix formalism can be written as:

$$\mathbf{K}_p = e^{i\kappa_p} = e^{-2i(u_p l + v_p m + w_p (n-1))}$$

Here,  $\mathbf{u}$  is defined in terms of wavelength. The visibility can hence be written (taking only the phase term into account)

$$V_{pq} = \mathbf{K}_p \mathbf{B} \mathbf{K}_q^H$$

The phase term is a scalar matrix, and hence can be moved around in the Jones chain.

---

<sup>3</sup>The net measured visibility is lowered in amplitude due to the presence of this complex term in the Jones matrix, which is variable in terms of both frequency and time. This effect is called “smearing”.

- The **source-independant antenna** gain term: The interferometer itself also has some corrupting effects, and these can be considered in the Jones chain in the form  $\mathbf{G}_p$ . This describes the Direction Independant Effects (DIEs) or the uv- Jones term.
- The **source-dependant** gain term: This is the remainder of the Jones chain of the form  $\mathbf{E}_{sp}$ . This represents the Direction Dependant Effects (DDEs) or the sky-Jones term.

Hence, in total, the Jones chain can be written as:

$$\mathbf{J}_{sp} = \mathbf{G}_p \mathbf{E}_{sp} \mathbf{E}_{sp} \quad (1.8)$$

The final visibility matrix can be written<sup>4</sup> as:

$$\mathbf{V}_{pq} = \mathbf{G}_p \left( \sum_s \mathbf{E}_{sq} \mathbf{K}_{sq} \mathbf{B}_s \mathbf{K}_{sq}^H \mathbf{E}_{sq}^H \right) \mathbf{G}_q^H \quad (1.9)$$

In LOFAR, this equation is taken over all the sufficiently bright sources in the horizon. However, sky is a continuous brightness distribution  $B(\sigma)$  with  $\sigma$  being the unit direction vector. Hence, the total visibility for the interferometer should be in the form of an integration, not as a summation of discrete sources. When we write the visibility matrix in terms of the plane projection as described earlier (as opposed to the unit spehere integral, which is not very traceable) it is of the form:

$$\mathbf{V}_{pq} = \mathbf{G}_p \left( \int_l \int_m \frac{1}{n} \bar{\mathbf{E}}_p(l, m) B \bar{\mathbf{E}}_q^H(l, m) e^{-2\pi i(u_{pq}l + v_{pq}m + w_{pq}(n-1))} dl dm \right) \mathbf{G}_q^H \quad (1.10)$$

Decomposing  $w_{pq} = w_p - w_q$  and writing the non-coplanetary term as per antenna terms, we can substitute  $W_p = \frac{1}{\sqrt{n}} e^{-2\pi i w_p(n-1)}$  and write  $\mathbf{E}_p = \bar{\mathbf{E}}_p W_p$ . This would give us the visibility matrix in the form of a 2D Fourier Transform of the apparent sky brightness for the baseline  $pq$  (with the term  $B_{pq}$  in the place of  $\mathbf{E}_p B \mathbf{E}_q$ ).

$$\mathbf{V}_{pq} = \mathbf{G}_p \left( \int_l \int_m B_{pq} e^{-2\pi i(u_{pq}l + v_{pq}m)} \right) \mathbf{G}_q^H \quad (1.11)$$

This is the general form of the **Van Cittert Zernike theorem**. This is the formalism used by the LOFAR calibration software. This equation effectively takes care of the direction dependant effects.

### 1.1.3 Overview of imaging procedure for LOFAR

In this section, a brief overview of how the data from the CEP cluster is imaged is given. The pipeline and the procedure I have used my differ slightly from the procedure given in this section.

The data from the CEP clusters is in the form of measurement sets. This data undergoes **pre-processing**. In this stage, the data is flagged in both time and frequency domains (even averaging of data may be done in both domains at this stage, if need be). After this, demixing is done. This is the subtraction of the brightest sources in the low frequency sky (the A-team<sup>5</sup>). A round of initial calibration is applied, which is done using a standard flux calibrator reference source. Then an initial phase calibration is performed. The Local Sky Model (LSM) used for this is obtained from the Global Sky Model (GSM). This uses 4 major catalogues: VLA Low-frequency Sky Survey (VLSS) (?), Westerbork Northern Sky Survey (WENSS) (?), the NRAO VLA Sky Surveyand (NVSS) (?) and the Multifrequency Snapshot Sky Survey (MSSS) (?). For removing any remaining RFI/ noise, another round of flagging and filtering is done.

After the pre-processing of the data, the **imaging** procedure is started. The non-coplanarity effects (the  $\mathbf{w}$  term of the equation 1.10) are removed using an algorithm, especially when doing wide field imaging. This is followed by taking care of the antenna primary beam variations which depend on the time, frequency and polarization. After this, a source finding algorithm is used to generate an updated LSM. Finally, a final round of flagging, imaging and LSM model updating is done. The final image products are then made available in the LTA.

<sup>4</sup>This equation is in the “onion form”. In this way, the various effects/corruptions are sequentially applied to the signal

<sup>5</sup>Cassiopeia A, Cygnus A, Taurus A, Virgo A, Hydra A, and Hera A

### 1.1.4 Importance of low frequency astronomy (LOFAR Key Science Projects)

LOFAR covers frequencies from 10 MHz to 250 MHz. As can be seen from Spectral Energy Distribution (SED) plot in the Fig. 1.4., the radiation in this regime is from non-thermal synchrotron emission<sup>6</sup>. Furthermore, the intensity of synchrotron radiation increases at such low frequencies, and hence, it gets easier to study the radiation from these low energy cosmic ray electrons. It is also interesting to note that low frequency radiation is produced by low energy electrons that have not been affected much energy loss, and hence are the older ones that have travelled farther from their point of origin (such as Supernova Remnants). Therefore, they can help us study galactic disks and the haloes of galaxies. In this section, the different Key Schience Projects (KSPs) undertaken by the LOFAR community are explained.

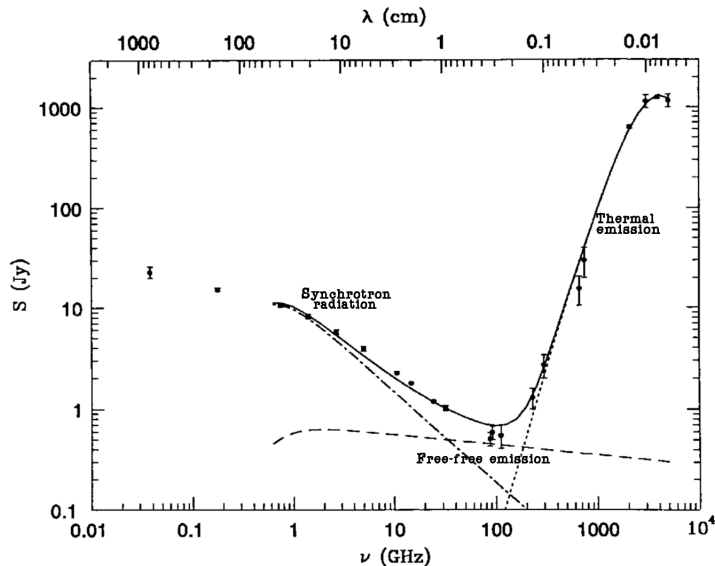


Figure 1.4: This is the Spectral Energy Distribution of M82, a starburst galaxy. The region below the frequency of 30 GHz is from non-thermal, synchrotron emission from cosmic ray electrons. Below that frequency, free-free emission from HII regions dominates, until  $\sim 200$  GHz (?).

**Epoch of Reionisation KSP:** According to the  $\Lambda$ CDM model, there existed a stage 400,000 years after the Big Bang, when the universe became transparent leaving only a relic radiation which we now call the Cosmic Microwave Background radiaion. This era came to be known as the “Dark ages”, and happened when the ions and electron combined. It came to an end 400 million years later, when objects such as stars and Black Holes were formed, and assembled into proto-galaxies. This era came to be known as the “Epoch of Reionization”, or “Cosmic dawn”. Several questions still need to be answered about the formation of the universe, such as what resulted in the end of the Dark Ages, and what gave rise to the EoR, and how are Black holes formed? One of the best ways to understand and answer these questions is by studying redshifted HI 21 cm emission line using LOFAR core elements.

**Surveys KSP:** LOFAR can be used for large sky surveys owing to its large instantaneous field of view. These surveys can help us study high redshifted galaxies (which will help us understand the formation and evolution of massive galaxies), clusters of galaxies (which will help us understand the charecteristics of magnetic fields and CR acceleraration) and cosmic star formation history of universe.

**Transients KSP:** This entails the study of transients such as pulsars, Gamma-Ray Bursts, X-ray binaries, radio supernovae and flare stars. Due to LOFAR’s wide field and good sensitivity, it would help us do extensive time-domain studies, and discover new transient events.

**Cosmic Rays KSP:** The Cosmic Ray (CR) flux follows the simple power law:  $\frac{dN}{dE} \propto E^{-\gamma}$ . Hence, for energies above  $10^{19}$ eV, only one particle per century per square kilometer reaches Earth. Hence, large effective areas are

<sup>6</sup>We will visit this in section 1.2.1.

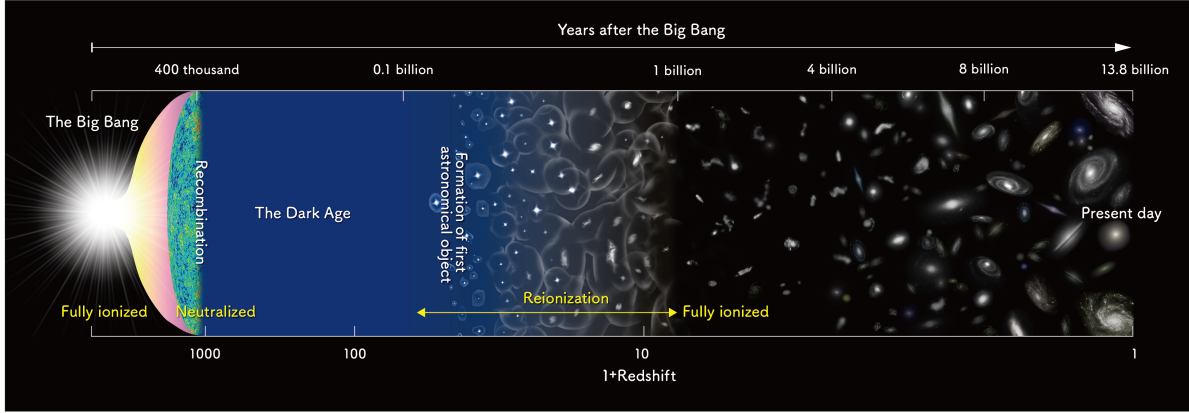


Figure 1.5: This is a schematic diagram depicting the lifetime of our universe. At redshift  $z \approx 1100$ , the dark ages begin, and EoR begins at  $z \approx 6-12$ . Courtesy of National Astronomical Observatory of Japan (NAOJ).

required to do proper statistics. At the energy of  $\sim 5 \times 10^{15}$ ,  $\gamma$  changes from 2.7 to 3.1 in the CR spectrum, and is called the “knee” of the spectrum. After this “knee”, the composition of the CRs is not well known. This knowledge can be obtained with the help of LOFAR, which will help us understand the acceleration and propagation mechanisms, and figure out the universal acceleration process. One of the candidates for the acceleration process is the diffusive shocks in the radio lobes of radio galaxies. Furthermore, extensive research on air showers at ground level, can help us study new particle physics.

**Solar KSP:** Sun is an intense source of radio thermal emission, and gives rise to solar flares and Coronal Mass Ejections (CMEs) which can be studied with the help of LOFAR. Sun also has an effect on the space environments, and communication technology on earth, and hence, this project mainly aims to study the space weather and solar physics.

**Cosmic Magnetism KSP:** Magnetic fields are very important to understand the Universe. LOFAR, due to its wide bandwidth can help us do best precision studies of Faraday rotation and weak magnetic fields. With the help of Faraday tomography/ Rotation Measure (RM) Synthesis can help us obtain polarized radio synchrotron emission. This topic will be visited again in Section ??.

## 1.2 Mechanisms important at Low Frequencies

In addition to the radiation from line emission (such as HI 21cm line), we have several other astrophysical processes that give rise to radiation. In this section, we will take a look at these processes.

### 1.2.1 Synchrotron emission:

When charged particles (mostly electrons) move around magnetic field lines at relativistic speeds, they emit photons. This emission of photons is called synchrotron emission and is non-thermal, as these relativistic electrons have a power law energy distributions:

$$N(E) dE = E^{-p} dE \quad (1.12)$$

Here,  $N(E) dE$  is the number of electrons per unit volume in energy interval  $E$  and  $E + dE$ , and ‘ $p$ ’ is the electron spectral index.

Let us consider a single electron (since synchrotron emission mostly comes from accelerating electrons), moving with velocity  $\mathbf{v}$  in a magnetic field  $\mathbf{B}$ . The electron energy is given by  $E = \gamma mc^2$ , where  $\gamma$  is the Lorentz factor and  $c$  is speed of light, and  $m$  is mass of electron. Its motion can be described by:

$$\frac{d}{dt}(\gamma m \mathbf{v}) = \frac{e}{c}(\mathbf{v} \times \mathbf{B}) \quad (1.13)$$

If we resolve  $\mathbf{v}$  into components parallel and perpendicular to the magnetic field represented as  $\mathbf{v}_{\parallel}$  and  $\mathbf{v}_{\perp}$ , then  $\mathbf{v}_{\parallel}$  remains constant with respect to time, and  $\frac{dv_{\perp}}{dt} = \frac{e}{\gamma m c} (\mathbf{v}_{\perp} \times \mathbf{B})$ . The electron thus moves in a helical path centered at the magnetic field lines. The pitch angle,  $\theta$ , of the trajectory of electron can be easily obtained from the velocity components. The angular gyrofrequency is given by the equation:

$$\omega_g = \frac{eB}{\gamma m} \quad (1.14)$$

From the figure 1.6, we can see that the electron will radiate in the Lorentz transformed beam pattern, and the forward power is in the beam of the angle  $\frac{\theta}{\gamma}$ .

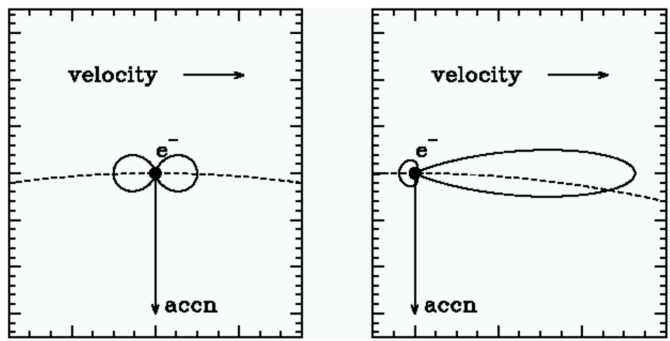


Figure 1.6: When an electron moves at relativistic speeds, the  $\sin^2$  radiation pattern is Lorentz transformed. *Left:* The radiation pattern of a non-relativistic electron. *Right:* The relativistic radiation pattern. This image has been taken from <http://www.astro.utu.fi/~cflynn/astroII/14.html>

The full derivation of the emission spectrum for a single electron can be seen in (?). Here, I have merely written down the final equation.  $I_{\parallel}$  and  $I_{\perp}$  represent the polarisations of the emission and  $T_r$  represents the period of the electron in orbit.

$$j(\omega) = \frac{I_{\parallel} + I_{\perp}}{T_r} = \frac{\sqrt{3}e^3 B \sin\theta}{8\pi^2 \epsilon_0 cm} \quad (1.15)$$

Here,  $F(x) = x \int_x^{\infty} K_{\frac{5}{3}}(z) dz$  where  $K_{\frac{5}{3}}$  is the modified Bessel function of the order  $\frac{5}{3}$  and  $x = \frac{2\omega a}{3c\gamma^3}$ . From this equation, one may find the emission from a population of electrons which is seen in synchrotron emission. For the distribution of electron described earlier, the total emission for electrons with a constant pitch angle can be given by:

$$J(\omega) \propto \kappa B^{\frac{(p+1)}{2}} \omega^{-\frac{(p-1)}{2}} \quad (1.16)$$

Hence, the spectral index of synchrotron emission is represented as  $\alpha$  and is equal to the power on the omega function.



# Chapter 2

## Imaging

In this thesis, we have imaged two galaxies- IC 342 and NGC 628, using the HBA data.

### 2.1 NGC628

NGC628 is an almost face-on grand design late-type spiral galaxy. It is located at a distance of almost 7.3 Mpc (?). Details on the galaxy can be found in the Table 2.1. It has two clearly defined spiral arms that can be seen in any optical image of the galaxy. In the UV, the spiral arms can be seen as bright knots on diffuse emission (?), and these knots are also traced in the H $\alpha$ . It is an isolated galaxy, and does not have strong density waves. HI holes have been detected in the HI layer of the galaxy, with sizes ranging from 0.24 kpc to 2 kpc (?). The galaxy is seen to consist of two disks, the inner disk being 8-10 kpc. These regions span different type of stellar populations (?), with a colder inner region (?), and faint H II regions covering the outer part of the galaxy (?). The H I distribution is seen to be extended and asymmetric to the southwest. In (?), it was seen that the inner part of the galaxy has a flat differentially rotating disk while the outer part is not a “well-behaved” disk. In (?) it was concluded that the inner part of the galaxy has no dust lanes, while outer part of the galaxy has clear nuclear dust spirals.

Distance <sup>1</sup>	~7.3 Mpc
Position <sup>2</sup>	RA:01h36m41.74s DEC:+15d47m01.1s
Morphology <sup>3</sup>	SA(s)c
Star Formation Rate <sup>4</sup>	1.21 $M_{\odot}$ /year
Inclination angle- inner disk (deg) <sup>5</sup>	7
Inclination angle- outer disk (deg) <sup>6</sup>	13.5
Position angle (deg) <sup>7</sup>	02

Table 2.1: Parameters of NGC628

### 2.2 IC342

IC 342 is an intermediate, almost face-on spiral galaxy of the Maffei 1/IC 342 group, the galaxy group nearest to our Local group, at a distance of around 3.3 Mpc(?). Details on the galaxy can be found in the Table 2.2. There has been a great amount of interest in the study of the galaxy, as it has a structure most similar to our own galaxy with similar dynamical mass ( $2 \times 10^8 M_{\odot}$ ) (?). The super massive black hole mass at the center of IC 342 is also of the same order ( $\sim 10^6 M_{\odot}$ ) as Milky Way. It is only 10.6 deg above the galactic plane, and is not clearly visible because of the Galactic disk and the large number of foreground stars in optical regime. It is the third largest spiral galaxy in the sky, with an angular size of . It consists of a central nuclear star cluster, where a lot of the star formation occurs. There exist five prominent Giant Molecular Clouds (GMCs) in the molecular ring and the arms, each of the mass of approximately  $10^6 M_{\odot}$  (?). The nucleus of the galaxy consists of two mini-spiral arms that are connected to the inner molecular ring. This structure is seen due to the presence of barred potential,

Position <sup>9</sup>	RA:03h46m48.503s DEC:+68d05m46.92s
Distance <sup>10</sup>	$\sim 3.3$ Mpc
Morphology <sup>11</sup>	SAB(rs)cd
Star Formation Rate <sup>12</sup>	$2.8 \text{ M}_\odot/\text{year}$
Inclination angle (deg) <sup>13</sup>	30
Position angle (deg) <sup>14</sup>	39.4
B <sub>T</sub> (mag) <sup>15</sup>	9.16

Table 2.2: Parameters of IC342

which is also indicated by the morphology of the velocity residuals<sup>8</sup> which showed the presence of a large bipolar structure (?). The outer part of the galaxy can be seen to have four distinct arms, with the inner part having speeds up to  $38 \pm 7 \text{ km s}^{-1}\text{kpc}^{-1}$  and the outer part ( $\sim 5$  kpc from center) having a speed of around  $11 \pm 6 \text{ km s}^{-1}\text{kpc}^{-1}$  (?). Photodissociation Region (PDR) is present within the central 400 pc of IC 342 (?). The physical and chemical geometry can be best understood from diagram 2.1 of IC 342. The yellow regions represent the H II regions. The star formation in the nuclear region was studied using Radio Recombination Lines (RRLs) and continuum emission at C- band and Ka-band with the JVLA, and two components were resolved lying east and west of the central star cluster, which were associated with two GMCs. It was predicted that several compact HII regions provide best fit for the two regions (?). It is at a low inclination of 31 deg, according to the HI kinematic data, which also indicates the counter-clockwise rotation of the galaxy (?). With the help of HII and SII filters, 16 Supernova Remnants were identified, most of them being near or in the H II regions and two of them isolated (?). IC 342 is also the host of four Ultra Luminous X-ray sources (ULX) (?).

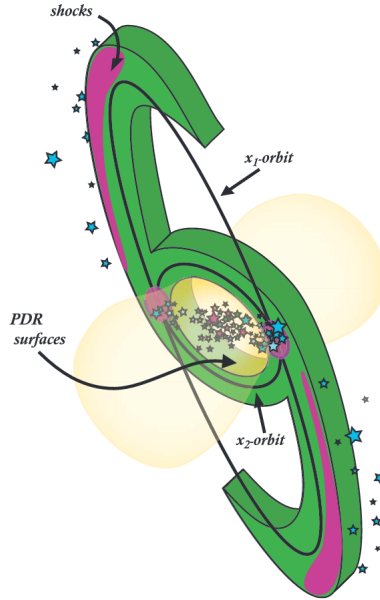


Figure 2.1: Schematic of the chemical and physical structure of the nucleus of IC 342(?)

Being an axis symmetric spiral (ASS), over the years, magnetic fields in this galaxy have been studied at several wavelengths- 6.2 and 11 cm (?), at 20 cm (?). Recently, Faraday tomography of the local ISM with LOFAR, in (?), showed the presence of two Faraday thin neutral clouds clearly separated in Faraday depth. In this thesis, we have also studied the polarized sources in the field of view of the galaxy at frequencies as low as 150 MHz. More information about the magnetic fields in IC342 can be found in section ??.

<sup>8</sup>Subtracting the the rotation model with the observed velocities gives the residual velocities

## 2.3 Observational setup

**NGC628:** The observations for NGC628 were done in an interleaved mode. The calibrator used was 3C 48, and the scans were alternatively taken from the target to the calibrator. The observation used 14 remote stations and 23 core stations. The number of stations used for the observation of NGC 628 was 37. No international stations were used. Details of the observation can be found in the table 2.3. The baselines used for the observation can be seen in figure ?? that shows the uv distance in meters and amplitude plot.

Start date (UTC)	22-Nov-2013 / 15:19:00.0
End date (UTC)	23-Nov-2013 / 00:50:59.9
Interleaved calibrator	3C48
Scan length on calibrator	2 min
Scan length on target	20 min
Duration of observation	9 hours 32 min
Final time on target	8 hours (24 scans)
Frequency range (from Pre-factor)	110.667-179.027 MHz
Frequency range (for Factor)	110.667-169.239 MHz
Total bandwidth on target	68.36 MHz
Final bandwidth in target	58.57 MHz

Table 2.3: Parameters of NGC628

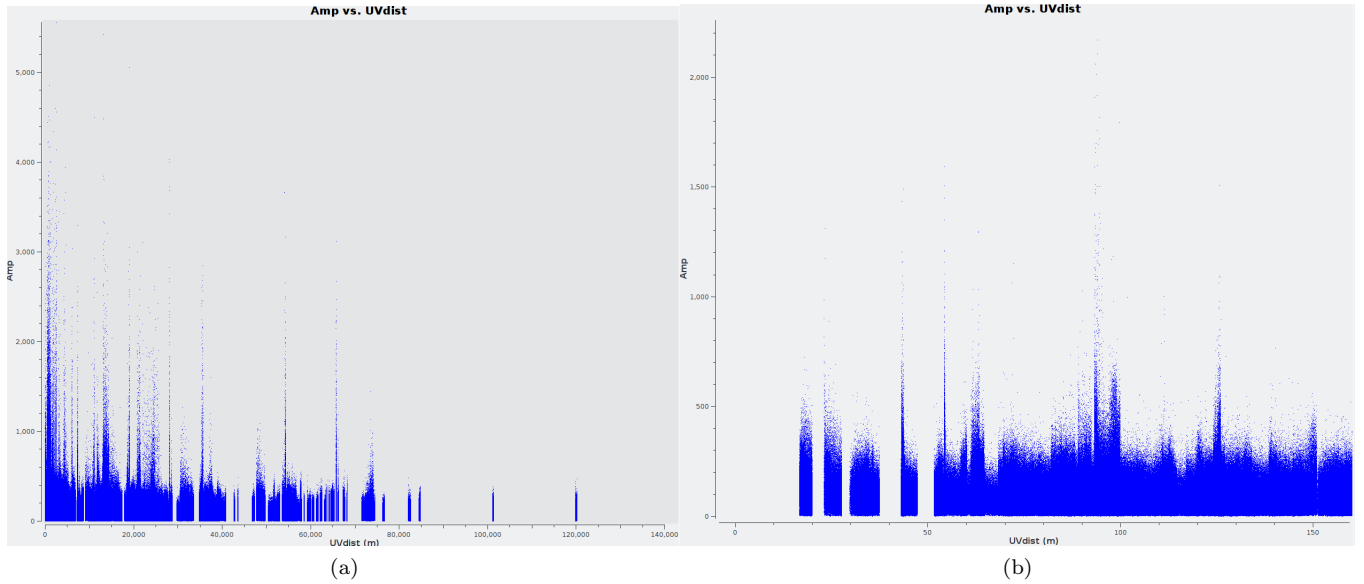


Figure 2.2: This was the arrangement of baselines used for the observation. This is a plot generated by task in CASA called 'plotms' for the first measurement set for the frequency 111 MHz in the first time step. From the plot, one can see the baselines used in terms of meters. As can be seen, the observation uses a dense core to image diffuse flux in the galaxy-the disk and the halo parts. *Right:* This image shows the shorter baselines used. The shortest projected baseline used was around 23 m.

## 2.4 Calibration of LOFAR data

Calibration in LOFAR is especially difficult due to the ionosphere that causes delay differences between antenna stations. This gives rise to additional phase errors in the visibilities that vary station to station due to LOFAR's large array size. This phase depends on two factors: (1) Free electron column density along the line of sight, (2) Frequency being observed. Another aspect to be noted while calibration of LOFAR is the station beam shape that varies with time and also, the difference between the beam model and the actual beam shape.

Inorder to take care of these effects, LOFAR data calibration involves two major parts. In this thesis, a tool called Factor<sup>16</sup> was used. The major steps to the data reduction are explained below. An overview on how to use the tool itself is described in a later section ??.

### 2.4.1 Direction independant part

The first step to do direction independant calibration is the flagging of RFI (Radio Frequency Interference) with the help of `AOFlagger` (?). Then, the data is averaged using `NDPPP` to be 4s in time resolution and 4 channels per subband in frequency resolution, to reduce the size of the data. Then, all baselines with CS013 HBA station were flagged and a flux density scale was created for 3C48 (which was chosen as the amplitude calibrator source) using the model that shows the flux density values of the source at several different frequencies, with a flux density of 64.76 Jy at 150 MHz. Using this primary beam calibrator, the gain solutions are obtained using `BlackBoard Selfcal` (BBS) for all four correlations. The gain solutions are then transferred to the target(?) data to correct for the instrumental effects<sup>17</sup>. The A team sources affect the visibilities through the side lobes of the station beam. Hence, the visibilities in which the contribution is more than 5 Jy (in apparent flux density) [ask Rainer] are flagged. This was followed by another round of flagging, and averaging. The data was concatenated into subbands with time resolution of 8 s. The width of each channel was kept at 48.828 kHz, and the total bandwidth was at 1.95 MHz. The last step in direction independant calibration involves the subtraction of soures by first subtracting clean components in medium resolution images, and then reimaging the subtracted image at a lower resolution (1.5' and uv cut range of 2 kλ) and full field of view image [write dimensions here]. This is done inorder to detect the extended flux emission and sources in the first and second side lobes. The new components found using the lower resolution image were again subtracted from the obtained visibilities. The clean components obtained from the two imaging steps in the direction independant part of calibration are convolved with the gain solutions and subtracted from the uncorrected visibilities and the obtained visibilities were used as input for the direction dependant calibration. Sky models for each frequency were generated (to take care of frequency dependance) which would be used in the later steps of factor.

### 2.4.2 Direction dependant part

From the figure 2.6, it can be seen that the artifacts from brighter sources severly affects the image quality. Hence, inorder to reduce the noise in the image due to ionosphere and the station beam effects, “faceting” is done obtain solutions and reach near-thermal noise limited images. The field of view is divided into a number of small isoplastic patches called facets. We assume that the calibration solution towards the brightest source in the facet can be used for the facet as a whole.

**For NGC628:** The visibilities obtained from prefactor were moved to the lofar4 cluster where the direction dependant calibration was to be done. The frequencies above 170 MHz were not taken for the next part, as they seemed to have bad visibilities. The first time step was also removed owing to corrupted visibilities. The first step to do DDE calibration is to make a list of the sources to make facets around. The sources above 100 mJy in

<sup>16</sup><https://github.com/lofar-astron/factor>

<sup>17</sup>**Instrumental effects:** The clocks at the remote stations are not perfectly synchronised, which causes a phase delay. This in addition to the phase delay by the ionosphere gives rise to phase errors. The phase difference for a baselines can be written as:

$$\Delta \text{ phase}(\nu, t) = \underbrace{2\pi p_0(t)\nu}_{\text{Clock difference effects}} - \underbrace{\frac{8.448 \times 10^9 p_1(t)}{\nu}}_{\text{Total Electron Content (TES) effects}} \quad [\text{rad}]$$

Here  $\nu$  represents frequency and  $p_0$  and  $p_1$  represents the clock difference and TEC difference. These errors need to be removed. This is done with the help of a bright source with a high Signal to Noise ratio on all baselines. Brute force search is done to obtain clock and TEC initial guesses, as computing using the equation is not computationally feasable.

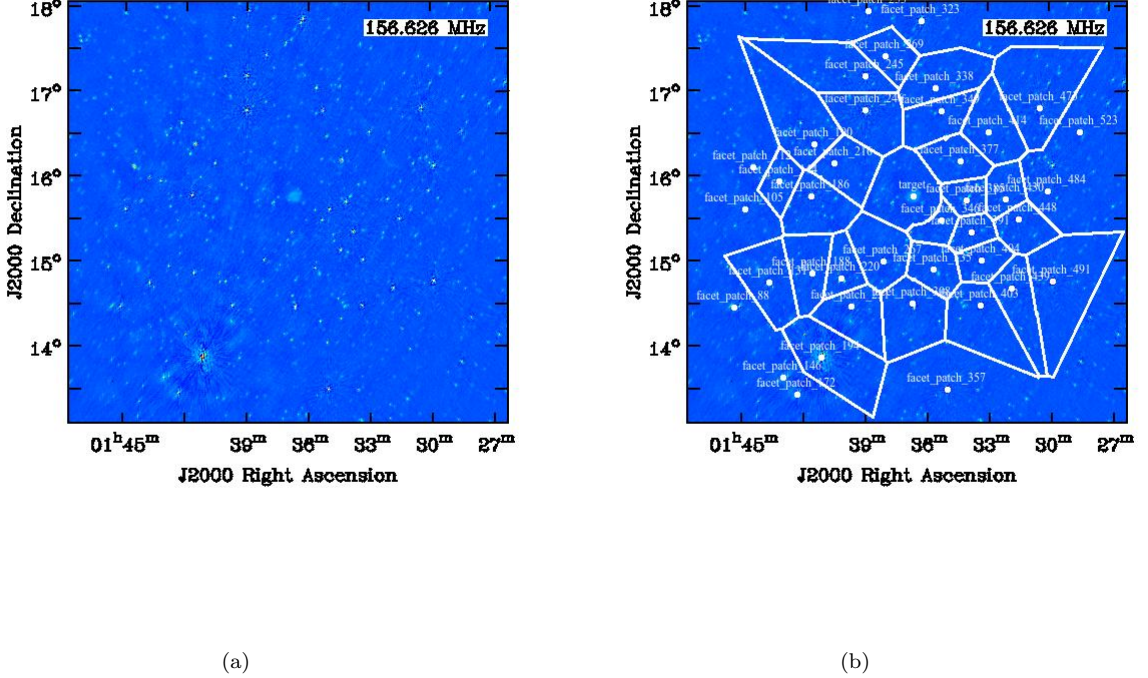


Figure 2.3: *Left:* Initial subtract image of NGC628, using frequencies between 135 to 167 MHz. It has a restoring beam of 43.99 arcsec by 31.64srcsec and position angle of -17.27deg. As can be seen, artifacts from individual sources, such as 3C 049 (at RA: 01h41m09.160s and DEC: +13d53m28.05s in J2000 coordinate system), can severely affect the galaxy image quality. Hence, the field of view is divided into “isoplastic” patches called “facets”. *Right:* The facet patches can be seen in the image, and are made around the radio sources present in each facet. They are represented by the white dots in the image on the right. The facet patches are based on the Veroni tessellation scheme.

apparent flux density were selected, with maximum size of 2.0'. They were set to be separated by a distance of at least 7'. In cases where more than one source was used as calibrators, the collective maximum flux was set to be 100 mJy. The faceting was done upto a radius of 2.8 deg<sup>18</sup>. If any sources were found at a higher radius than that, a small patch was made around this part. One such source was 3C 047, a quasar, which is labelled as source 1 in the figure 2.4. The boundaries for some of the sources had to be changed<sup>19</sup> to get better self calibration results (to remove the secondary sources in the facet). The calibration begin with source 194- commonly known as 3C49. The self-cal images after each iteration of 3C49 is shown in figure 2.5. To do the self- calibration, the source is first added back to the visibility data (the residual visibility obtained from DIE calibration), and phase shifted to the source in the facet, which in the fist case was 3C49. This is followed by the “short-timescale phase +TEC” calibration to take care of the ionospheric delay (row 2 in the figure 2.5). Then, to take care of the effects of the slowly varying station beam, the “slow gain” calibration is done. Then the imaging of the facet is done. Once the DDE calibration solutions for the facet are obtained, the other fainter sources within the facets are added back and corrected using the solutions of the strongest source that was used for the calibration. This is followed by the generation of an updated skymodel which is then subtracted from the residual visibilities with the obtained solutions. This whole process is then repeated for another facet that has the source with next highest flux density, so that the sources that have a higher calibration errors do not affect the DDE calibration of the fainter sources in other facets.

**For IC342:** The figure 2.7 shows the facets on the field of view of the observation, and the different directions in which the faceting was done. The sources above 300 mJy in apparent flux density were selected, with maximum

<sup>18</sup>This is by default at a value of  $\frac{FWHM \times 1.25}{2}$  of the primary beam at the higest frequency.

<sup>19</sup>Sources 246, 385, 335, 349, 267, 253, 477, 144

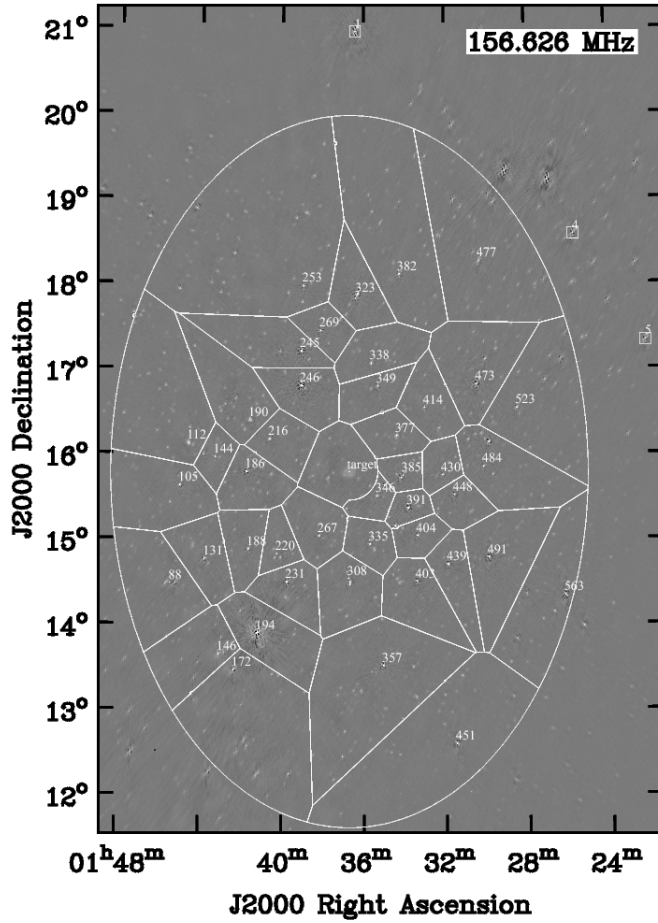


Figure 2.4: This image depicts the faceting scheme used for NGC628. The middle facet marked “target” is NGC628. The sources marked 1, 4 and 5 were included by hand due to their high fluxes. The image is the one obtained from the initial calibration (same as the one in the previous figure). The beam is elongated to account for the low elevation elongation of the LOFAR primary beam.

size of  $2.0'$ . They were set to be separated by a distance of at least  $7'$ . In cases where more than one source was used as calibrators, the collective maximum flux was set to be 200 mJy. The faceting was done upto a radius of 1 deg, while the sources for the directions were set to be searched up to  $7'$ . A directions file was made by factor based on the given parameters. Then, a few changes were made- the boundaries for some of the sources had to be changed to get better self calibration results (to remove the secondary sources in the facet). A few of the sources below the given flux density limit had to be given their own facets. There sources were marked with the prefix ‘d’. The rest of the procedure followed was mimicking the one for NGC628.

### 2.4.3 Overview of Factor

This section gives the description of the steps to calibrate LOFAR data with the help of Factor. Imaging, for both IC342 and NGC628 was done on interleaved datasets. Factor is used to produce deep images using the HBA data employing the direction dependant facet calibration method as described in (?). The first step to calibration, involves the preparation of the data, using a tool called Pre-factor<sup>20</sup>, which also does the **Direction independant calibration**.

*Step 1:* The data of the calibrator and target are kept in separate directories. The calibrator data is first processed using the Calibrator Pipeline. The gain solutions obtained using the calibrator are then used for the clock-TEC separation and to compute average gain amplitudes.

*Step 2:* The target data processing is done. This uses the Target Pipeline that adds the Rotation Measure cor-

<sup>20</sup><https://github.com/lofar-astron/prefactor/wiki>

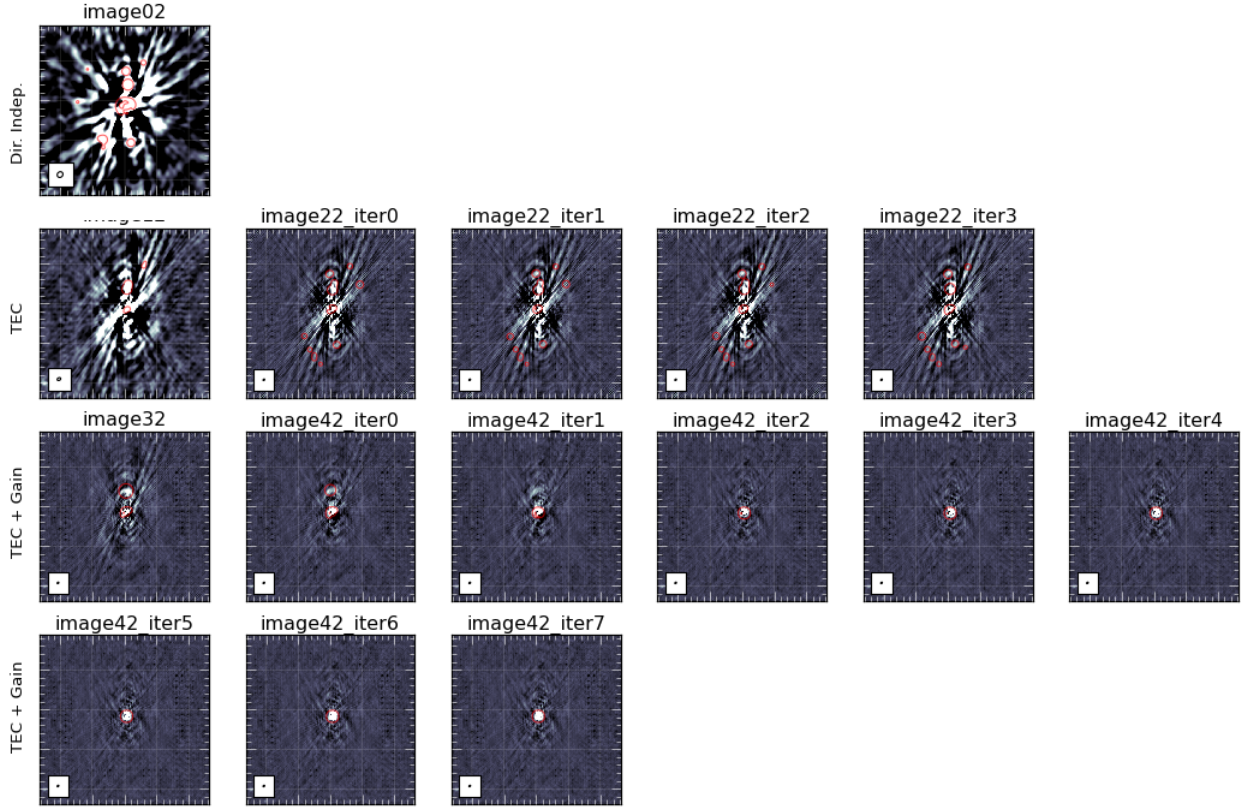


Figure 2.5: Self calibration images of the facet with source 194- otherwise known as 3C49. The image marked “Dir. Independ.” is the direction independant image of the facet. In the second row, the phase term is being solved, which took three iterations. Then, the phase + amplitude calibration was done, which took 7 iterations.

rection from RMextract to the data file (h5parms) from the Calibrator Pipeline. This requires files that contain information about the ionospheric electron content. It also pre-process the input measurement sets (MSs) and applies the values from the h5parms. It predicts and flags the A-team contamination, and sorts the MSs by time and frequency into groups that are later concatenated. It removes the files with too much flagged data. It also does phase-only calibration on the skymodel. It also produces diagnostic plots, that can be seen in the table 2.4. *Step 3:* The final part of Pre-factor is the “Initial subtract” pipeline that produces the sky-model required for Factor from the visibilities. Initial- subtract also gives the full field of view image. In our analysis, raw data was used (non-NDPPP-ed data: no demixing, averaging and flagging was done before-hand), which required the “Pre-Facet-Calibrator-RawSingle” parset (this option is not available in Prefactor anymore). The target part of the calibration was done in six batches due to the large size.

Once the data has been prepared using Prefactor, the **Direction Dependant calibration** is done.

*Step 1:* The Factor parset is prepared. In this, one can specify any additional flagging needed. One can also give instructions on the field in which faceting needs to be done, and the maximum size of facets and sources (or group of sources).

*Step 2:* The directions file can either be generated by Factor, or be edited by the user. One may also remove some of the directions, and add a few depending on what is needed. Factor is run using the command “runfactor”.

*Step 3:* One can check the progress of the Factor run, with the help of the command “checkfactor”. In Factor, various operations are simultaneously undertaken: Outliers and sources in each of the facets are peeled in the operations named “outlierpeel” and “facetpeel” respectively. This is followed by “facetselfcal” which self calibrates the facet calibrator. “facetsub” operation subtracts the model of the facet and calibrator. The imaging of the facet is done in the “facetimage” operation, in which the facet is imaged using full bandwidth, unlike in the “facetselfcal”,

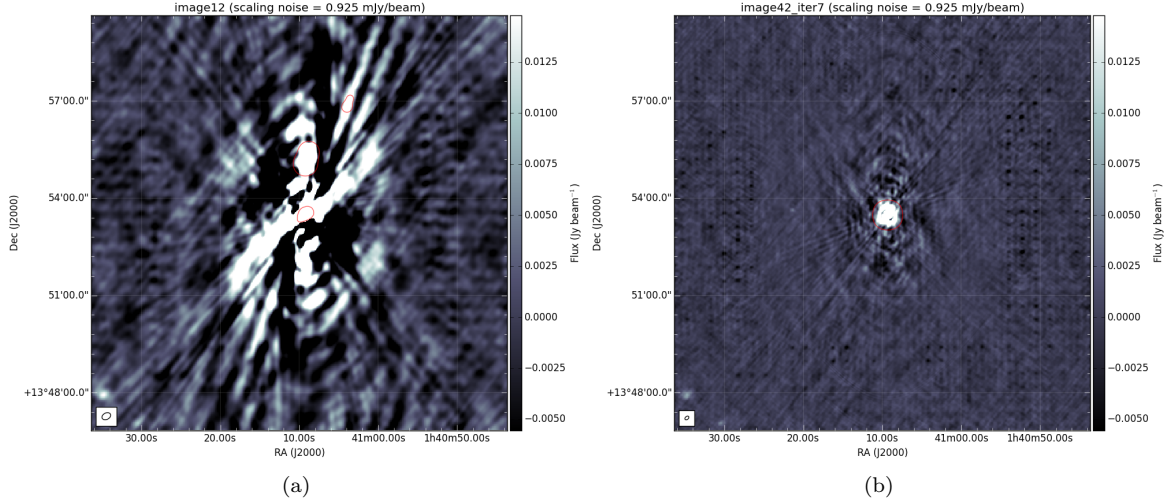


Figure 2.6: *Left:* The initial subtract image of facet containing the source 3C49. *Right:* Final self-cal image of 3C49. The image is considerably better than the one on the left, however some of the artifacts still remain. The source is the source is farther away from the target source, hence, the artifacts that remain do not affect the image too much.

in which only part of the bandwidth is used to image the facet. If the full field of view image is required, it can be done using the “fieldmosaic” operation, in which all the final facet images are made into a mosaic, after the primary beam attenuation correction. The main output of Factor is generated in the “results” directory, which contains the self-calibrated visibilities and the self-calibrated images of the different facets.

## 2.5 Imaging

Common Astronomy Software Application<sup>21</sup> was used to make images of the two galaxies. The visibilities of the target facet were used to make the images of both the galaxies. The LOFAR primary beam is much larger than the size of the galaxies, and hence, LOFAR primary beam correction was not done.

**For IC342 :** Three images of varying resolutions were made. The noise of each image was obtained from the rms value of a region around a part of the image with no source. The images were made using the multi-scale clean technique. The outer taper for the image in figure 2.8 was 14 arcsec by 9.5 arcsec. or figure 2.9, the outer taper was 22 arcsec by 22 arcsec, and for the image 2.10, the outer taper used was 23 arcsec by 24 arcsec.

---

<sup>21</sup><https://casa.nrao.edu/>

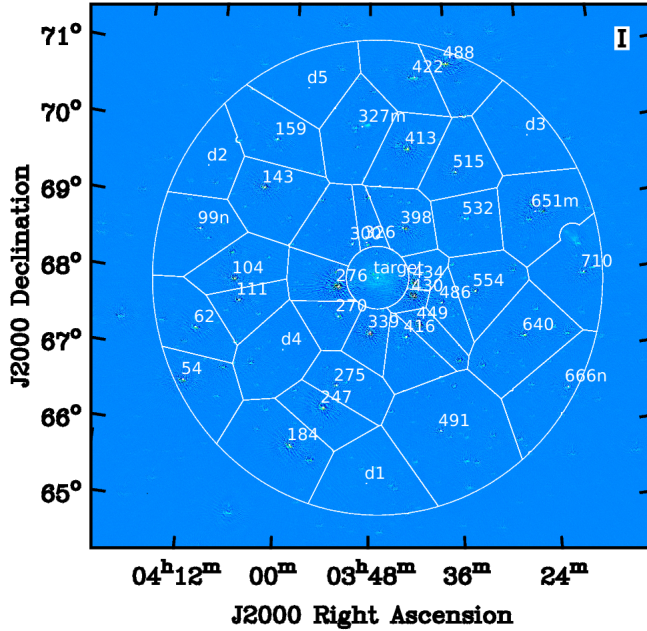


Figure 2.7: Faceting in IC342 for Direction Dependant calibration in Factor. The facets have been overlaid on the image made using averaged Prefactor data. The resolution of the image is 17.35 by 12.72 arcsec. It was cleaned to a threshold of 0.3 mJy with Briggs weighting of -0.5.

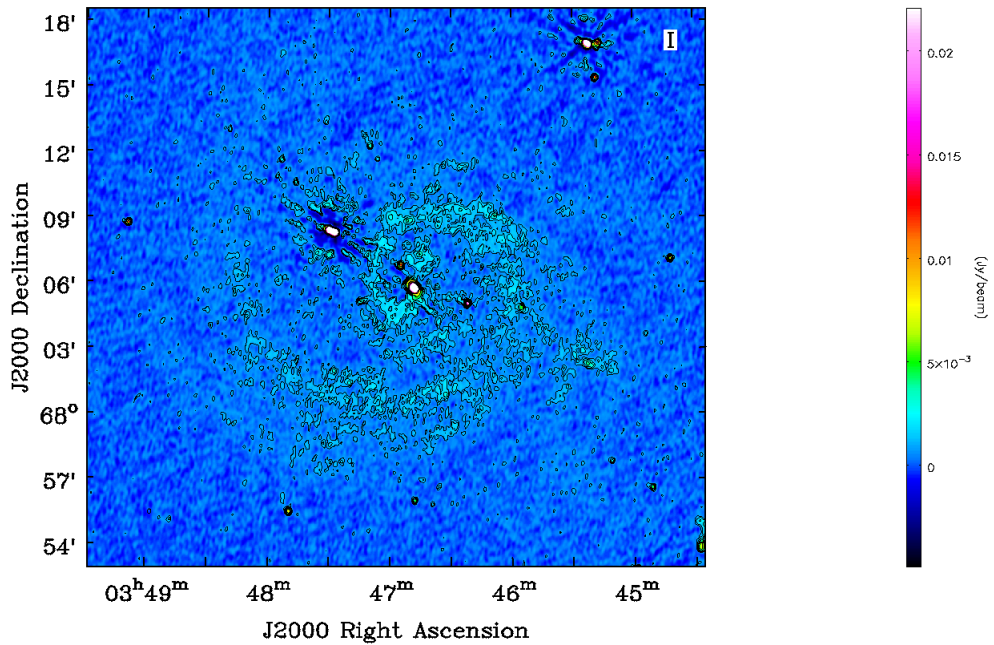


Figure 2.8: This is the LOFAR image of IC342 at the central frequency of 146.2 MHz. Bandwidth of the observation was 62.5 MHz. This image has the resolution of 12.48" by 10.26"; PA: -8.10 deg. The contours are at 3, 8, 12, 18, 18, 32 and 44 of 0.3 mJy/beam, which is the noise of the image in a quiet region.

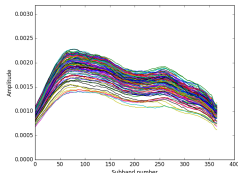
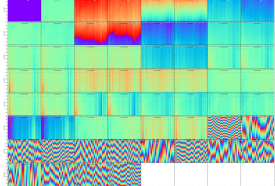
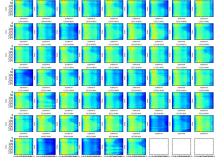
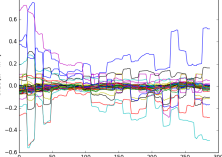
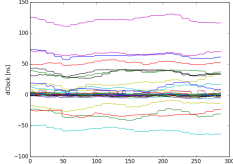
Diagnostic plots	Description
	This graph shows the amplitude solutions in the different subbands. As can be seen, there are no clear outliers, showing that this data set does not have bad amplitude solutions.
	This plot shows the calibrator solutions in the YY polarisation. The CS001HBA0 station is flagged, and some of the frequencies between 170 to 180 MHz seem to have noisy data.
	This shows the waterfall plots of the amplitude solutions for the single stations. It can be used to see which stations are bad in the first plot.
	This plot shows the differential Total Electron Content (dTEC). It shows that the data is fine, even though it may noisy.
	This plot shows the differential clock values. For all the core stations, the values should lie on 0.
	This plot gives the median difference of the phase solutions for the X and the Y antennas. For the station calibration, the X and Y dipole phases are not aligned with each other resulting in phase offsets. The blue spikes represent the ones that have been flagged by pre-factor.

Table 2.4: This table shows the diagnostic plots that are obtained as an output from the Prefactor pipeline. They give an overview of the condition of the data and help us select and flag any data sets that seem bad, and were not previously flagged by the pipeline.

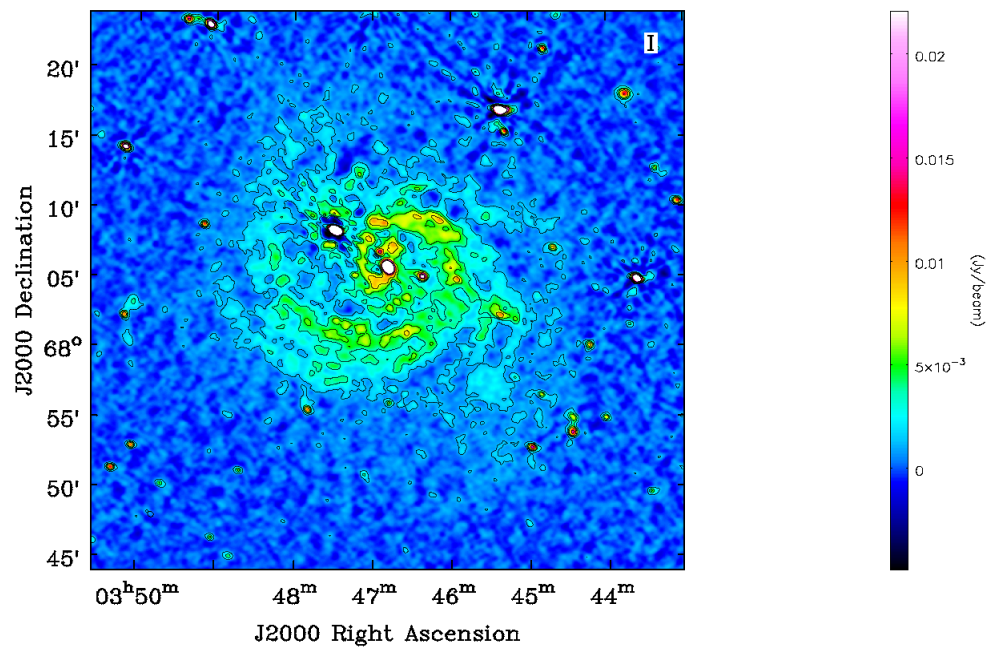


Figure 2.9: This image has the resolution of  $25.93''$  by  $23.26''$ ; PA: 62.7 deg. The contours are at 3, 8, 12, 18, 18, 32 and 44 of 0.43 mJy/beam.

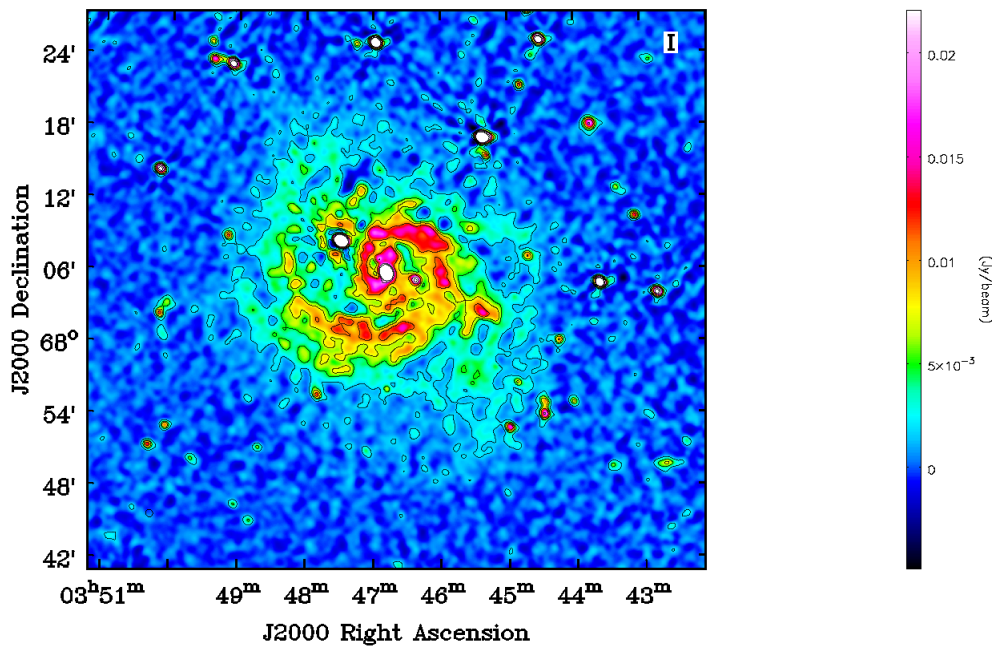


Figure 2.10: This image has the resolution of  $38.15''$  by  $34.39''$ ; PA: 23.99 deg. The contours are at 3, 8, 12, 18, 18, 32 and 44 of 0.6 mJy/beam.



## Appendix A

### Appendix not too long title

Lorem ipsum dolor sit amet, consectetur adipiscing elit. Etiam lobortis facilisis sem. Nullam nec mi et neque pharetra sollicitudin. Praesent imperdiet mi nec ante. Donec ullamcorper, felis non sodales commodo, lectus velit ultrices augue, a dignissim nibh lectus placerat pede. Vivamus nunc nunc, molestie ut, ultricies vel, semper in, velit. Ut porttitor. Praesent in sapien. Lorem ipsum dolor sit amet, consectetur adipiscing elit. Duis fringilla tristique neque. Sed interdum libero ut metus. Pellentesque placerat. Nam rutrum augue a leo. Morbi sed elit sit amet ante lobortis sollicitudin. Praesent blandit blandit mauris. Praesent lectus tellus, aliquet aliquam, luctus a, egestas a, turpis. Mauris lacinia lorem sit amet ipsum. Nunc quis urna dictum turpis accumsan semper.

Lorem ipsum dolor sit amet, consectetur adipiscing elit. Etiam lobortis facilisis sem. Nullam nec mi et neque pharetra sollicitudin. Praesent imperdiet mi nec ante. Donec ullamcorper, felis non sodales commodo, lectus velit ultrices augue, a dignissim nibh lectus placerat pede. Vivamus nunc nunc, molestie ut, ultricies vel, semper in, velit. Ut porttitor. Praesent in sapien. Lorem ipsum dolor sit amet, consectetur adipiscing elit. Duis fringilla tristique neque. Sed interdum libero ut metus. Pellentesque placerat. Nam rutrum augue a leo. Morbi sed elit sit amet ante lobortis sollicitudin. Praesent blandit blandit mauris. Praesent lectus tellus, aliquet aliquam, luctus a, egestas a, turpis. Mauris lacinia lorem sit amet ipsum. Nunc quis urna dictum turpis accumsan semper.

Lorem ipsum dolor sit amet, consectetur adipiscing elit. Etiam lobortis facilisis sem. Nullam nec mi et neque pharetra sollicitudin. Praesent imperdiet mi nec ante. Donec ullamcorper, felis non sodales commodo, lectus velit ultrices augue, a dignissim nibh lectus placerat pede. Vivamus nunc nunc, molestie ut, ultricies vel, semper in, velit. Ut porttitor. Praesent in sapien. Lorem ipsum dolor sit amet, consectetur adipiscing elit. Duis fringilla tristique neque. Sed interdum libero ut metus. Pellentesque placerat. Nam rutrum augue a leo. Morbi sed elit sit amet ante lobortis sollicitudin. Praesent blandit blandit mauris. Praesent lectus tellus, aliquet aliquam, luctus a, egestas a, turpis. Mauris lacinia lorem sit amet ipsum. Nunc quis urna dictum turpis accumsan semper.

Lorem ipsum dolor sit amet, consectetur adipiscing elit. Etiam lobortis facilisis sem. Nullam nec mi et neque pharetra sollicitudin. Praesent imperdiet mi nec ante. Donec ullamcorper, felis non sodales commodo, lectus velit ultrices augue, a dignissim nibh lectus placerat pede. Vivamus nunc nunc, molestie ut, ultricies vel, semper in, velit. Ut porttitor. Praesent in sapien. Lorem ipsum dolor sit amet, consectetur adipiscing elit. Duis fringilla tristique neque. Sed interdum libero ut metus. Pellentesque placerat. Nam rutrum augue a leo. Morbi sed elit sit amet ante lobortis sollicitudin. Praesent blandit blandit mauris. Praesent lectus tellus, aliquet aliquam, luctus a, egestas a, turpis. Mauris lacinia lorem sit amet ipsum. Nunc quis urna dictum turpis accumsan semper.

Lorem ipsum dolor sit amet, consectetur adipiscing elit. Etiam lobortis facilisis sem. Nullam nec mi et neque pharetra sollicitudin. Praesent imperdiet mi nec ante. Donec ullamcorper, felis non sodales commodo, lectus velit ultrices augue, a dignissim nibh lectus placerat pede. Vivamus nunc nunc, molestie ut, ultricies vel, semper in, velit. Ut porttitor. Praesent in sapien. Lorem ipsum dolor sit amet, consectetur adipiscing elit. Duis fringilla tristique neque. Sed interdum libero ut metus. Pellentesque placerat. Nam rutrum augue a leo. Morbi sed elit sit amet ante lobortis sollicitudin. Praesent blandit blandit mauris. Praesent lectus tellus, aliquet aliquam, luctus a, egestas a, turpis. Mauris lacinia lorem sit amet ipsum. Nunc quis urna dictum turpis accumsan semper.